Journal of MATERIALS RESEARCH

Article
DOI: 10.1557/jmr.2019.382

2D AND NANOMATERIALS

FOCUS ISSUE

Thermal expansion of nano–boron carbide under constant DC electric field: An in situ energy dispersive X-ray diffraction study using a synchrotron probe

Hülya Biçer[1,a)], Enver Koray Akdoğan[2], İlyas Şavklıyıldız[3], Christopher Haines[4], Zhong Zhong[5], Thomas Tsakalakos[2]

[1]Department of Metallurgy and Materials Engineering, Kütahya Dumlupınar University, Kütahya 43000, Turkey; and Department of Materials Science & Engineering, Rutgers University, Piscataway, New Jersey 08904, USA
[2]Department of Materials Science & Engineering, Rutgers University, Piscataway, New Jersey 08904, USA
[3]Deparment of Metallurgy and Materials Engineering, Konya Technical University, Konya 42250 Turkey
[4]US Army Research Laboratory, Aberdeen Proving Ground, Adelphi, Maryland 21005, USA
[5]National Synchrotron Light Source I & II, Brookhaven National Laboratory, Upton, New York 11973, USA
[a)]Address all correspondence to this author. e-mail: hulya.bicer@dpu.edu.tr

Received: 12 September 2019; accepted: 25 November 2019

The thermal expansion coefficient (TEC) of nano-B_4C having 50 nm mean particle size was measured as a function of applied direct current (DC) electric field strength varying from 0 to 12.7 V/mm and over a temperature range from 298 K up to 1273 K. The TEC exhibits a linear variation with temperature despite being measured over a range that is well below 50% of B_4C's normal melting temperature. The zeroth- and first-order TEC coefficients under zero-field condition are $4.8220 \pm 0.009 \times 10^{-6}$ K^{-1} and $1.462 \pm 0.004 \times 10^{-9}$ K^{-1}, respectively. Both TECs exhibit applied DC electric field dependence. The higher the applied field strength, the steeper the linear thermal expansion response in nano-B_4C, which suggests that the applied field affects the curvature of the interatomic potentials at the equilibrium bond length at a given temperature. No anisotropic thermal expansion with and without applied electric field was observed, although nano-B_4C has a rhombohedral unit cell symmetry. The rhombohedral unit cell angle was determined as $\delta_R = 65.7046°$ (0.0007), and it remains unaffected by a change in temperature and applied electric field strength, which we attribute to B_4C nanoparticle size and its carbon saturation.

Introduction

Thermal expansion is an important anharmonic solid-state property of materials [1, 2]. It is of particular importance for high temperature structural and mechanical applications where high thermal stability and high strength are required in a given engineering material for which the (stress-free) thermal strains need to be controlled. Fundamentally, the magnitude of the thermal expansion coefficient (TEC) is inversely related to the stiffness of the chemical bonds forming the solid of interest [1, 2].

Boron carbide (B_4C hereafter) is a highly covalent, non-oxide ceramic that has a high melting temperature (2763 °C at 1 atm), outstanding hardness (2400–2800 on Vickers scale), high neutron absorption cross section (760 barn at neutron velocity of 2200 m/s), and low density (3.15 g/cm^3) [3, 4, 5, 6, 7]. These unique combinations of properties make B_4C an attractive candidate in structural ceramic applications, such as armor, wear-resistant components, and nuclear reactor control rods, to name but a few [8, 9, 10, 11]. Extensive studies on the atomic structure of B_4C are available in the literature [2, 7, 8, 9]. In the $0.088 \leq x \leq 0.200$ C% compositional range, B_4C crystallizes as a single phase ($B_{1-x}C_x$) with a rhombohedral structure (D^5_{3d}–$R3$-m) as shown in Fig. 1. It consists of 15 atoms, of which 12 are situated on the corners of a deformed icosahedron, and the remainder is in the form of linear 3-atom chains. The atoms on icosahedra are connected with covalent bonds to atoms in neighboring icosahedra. The site occupancies of carbon and boron atoms are still controversial because the electronic scattering cross sections of boron and carbon isotopes are similar. As such, most structure solution to date

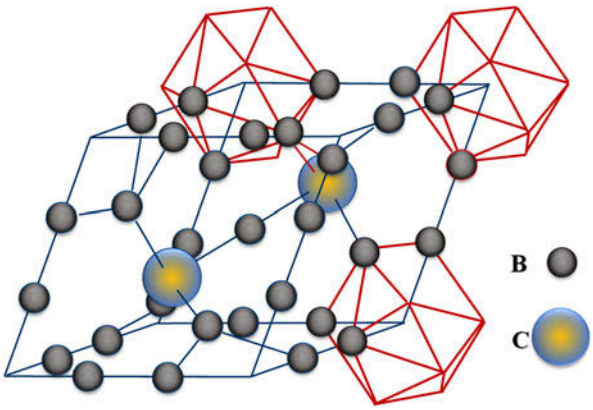

Figure 1: Crystal structure of rhombohedral B_4C (space group *R3-m*). The structure consists of 15 atoms, of which 12 are situated on the corners of a deformed icosahedron, whereas the remainder is in the form of linear 3-atom chains. The atoms on icosahedra are connected with covalent bonds to atoms in neighboring icosahedra.

remained inconclusive [7]. However, the currently accepted stable phase of B_4C, which contains 20 mole % carbon, is identified with B12 (CCC) chain configuration. On the other hand, the rhombohedral lattice parameters for carbon-rich B_4C compound are a = 5.16 Å and α = 65.7°, with minor variations depending on the synthesis conditions and such [2, 7]. The lattice parameters of the rhombohedral boron carbide unit cell can be computed from parameters of the hexagonal unit cell, which is considered to be easier than solving the complicated rhombohedral system. In the hexagonal system, the lattice parameters of B_4C are a_0 = 5.60 Å and c_0 = 12.07 Å, resulting in an axial ratio of c_0/a_0 = 2.155 [8, 9]. Moreover, the size of boron and carbon atoms is close enough so that they can substitute for each other. If that happens, the unit cell of boron carbide shrinks slightly as boron is replaced by carbon [8, 9].

The thermal expansion behavior of boron carbide has been reported in several articles [12, 13, 14]. The average TEC in the 298–1073 K temperature range is reported as 4–8 $\times$ 10^{-6} K^{-1} in Thevenot's review article [12], whereas Pilladi et al. reported that the average TECs in the 298–1773 K temperature range for nano- and microcrystalline boron carbides are 7.76 $\times$ 10^{-6} K^{-1} and 7.06 $\times$ 10^{-6} K^{-1}, respectively [14]. Both of these landmark articles report a TEC that is not temperature dependent over the temperature ranges of interest [14, 15, 16]. The reported TEC data for engineering materials are typically determined under constant pressure and zero electric field. However, we carried out experiments under various electric fields in this study to observe if there were a correlation between applied electric field and thermal expansion behavior in B_4C. Such a study is not available to the best of our knowledge. Our motivation arose from the recent advances in electric field–assisted sintering techniques, such as spark plasma sintering [17, 18] and flash sintering [19, 20]. Such novel sintering techniques necessitate the assessment of the electric field response of a material of interest, although it is concomitantly subjected to a thermal field. Specifically, the assessment of the electric field response of a material such as B_4C under a thermal field is of great importance because of the strong covalent character of its chemical bonding. That is so because the atomic mobility of the species in such highly covalent ceramics is intrinsically very low, leading to very poor solid-state diffusion kinetics [17, 18, 19, 20]. Consequently, densification of covalent ceramics such as B_4C is challenging, unless very expensive techniques such as hot pressing is used, which the said electric field–assisted methods will likely replace in due course [17, 18, 19, 20]. Insights into the thermal expansion behavior under an applied electric are needed for understanding the electric field–induced densification of B_4C such as in flash sintering. That is so because one needs to be able to discern the lattice expansion due to flash sintering from the TEC-induced lattice expansion which is intrinsically present as a baseline [20].

Here, we have focused on nano-B_4C as nano-particulate solids are of current scientific and of technological interest. We have confined our study to a temperature range in which nano-B_4C exhibits insulator behavior so that thermal expansion under a constant electric field can be thermodynamically defined. We have brought to bear energy dispersive X-ray synchrotron diffraction in the Laue mode to probe the thermal expansion behavior of nano-B_4C under an applied electric field because this technique is ideally suited for such an in situ assessment. Specifically, the said technique enables one to collect a large ensemble of data very rapidly and with high accuracy. In what follows, we will show that there is indeed a correlation between thermal expansion and an applied DC electric field in nano-B_4C, which was discovered thanks to energy-dispersive X-ray synchrotron diffraction in the Laue mode.

This article is organized as follows: In Phenomenological Model and Theory, we present the crystallographic model and thermodynamics formalism that we developed by which we analyze our data and represent the results. In Results, we present the results and a discussion. First, we elaborate on the observed data and also provide an analytical representation of the electric field dependence of the TECs (linear and non-linear). Second, we provide a self-consistent discussion on the observed electric field–dependent nonlinear thermal expansion behavior using fundamental concepts in solid-state theory. In Conclusions, we present some closing remarks, wherein we also propose future work in this line of research. In Experimental Methods, we provide a detailed account of the advanced energy-dispersive diffraction method, which we used in this study because it is less known than Bragg–Brentano parafocusing methods.

Phenomenological model and theory

The rhombohedral lattice parameter (a_R) and unit cell angle (δ_R) of nano-B_4C were computed from d-spacing data using the UnitCell software package [21]. The said d-spacing data were first computed using the diffracted energies E_{hkl} (see Experimental methods), which was obtained through peak fitting. We used (101), (003), (012), (110), (104), and (021) Bragg reflections in obtaining (a_R) and (δ_R). Pre-estimation of lattice parameters was not needed as we used a nonlinear least-squares method [21]. The rhombohedral unit cell volume (V_R) was computed from $V_R = a_R^3\sqrt{1-3\cos^2(\delta_R)+2\cos^3(\delta_R)}$ [22]. The standard deviation in the lattice parameter data was <0.0009 Å.

At a given applied DC electric field strength (including E_o = 0 V/mm), the temperature dependence of the nano-B_4C lattice parameter (a_R) was modeled with a second order (parabolic) Taylor expansion of the form (also see Table I)

$$a_R^E(T) \approx a_R^{E_o}(\theta)_E + \left(\frac{\partial a_R^E(\theta)}{\partial T}\right)_E [T-\theta] + \left(\frac{1}{2!}\frac{\partial^2 a_R^E(\theta)}{\partial T^2}\right)_E [T-\theta]^2 \quad , \tag{1}$$

from which the linear TEC at constant DC electric field strength α_L^E can simply be obtained from its thermodynamic definition as a phenomenological equation [1].

$$\alpha_L^E(T) \simeq \left(\frac{1}{a_R^{E_o}(\theta)}\right)\left(\frac{\partial a_R^E(T)}{\partial T}\right) \quad , \tag{2}$$

as

$$\alpha_L^E(T) \simeq \alpha_1 + \alpha_2[T-\theta] \quad , \tag{3}$$

where

$$\alpha_1 \simeq \left(\frac{1}{a_R^{E_o}(\theta)}\frac{\partial a_R^E(\theta)}{\partial T}\right) \text{ and } \alpha_2 \simeq \left(\frac{1}{a_R^{E_o}(\theta)}\frac{\partial^2 a_R^E(\theta)}{\partial T^2}\right) \quad , \tag{4}$$

In Eqs. (1)–(4), T is the absolute temperature, θ is the reference temperature which is 298 K in this study, and $a_R^{E_o}(\theta)$ is the rhombohedral unit cell parameter at 298 K and zero applied DC electric field strength, i.e., E_o = 0 V/mm. As will be presented in Results, we have determined α_1 and α_2 as a function of applied DC electric field strength over the temperature range of interest. In other words, we have evaluated $\left(\partial\alpha_1/\partial E\right)_T$ and $\left(\partial\alpha_2/\partial E\right)_T$, and, thereby, modeled $\alpha_L(T, E)$ as a convoluted Taylor expansion

$$\alpha_L^E(T) \simeq \alpha_1(E) + \alpha_2(E)[T-\theta] \tag{5}$$

whereby we obtained a phenomenological theory of electric field dependence of the TEC for B_4C (See Results for details).

TABLE I: Electric field dependence of nano-B_4C lattice parameter.

Electric field (V/mm)	Temperature range (K)	Temperature dependence of lattice parameter (Å)
0.0	298–1010	$a(T) = 5.1684 + 2.492 \times 10^{-5}(T-298) + 3.778 \times 10^{-9}(T-298)^2$
5.3	298–875	$a(T) = 5.1684 + 12.663 \times 10^{-5}(T-298) + 1.131 \times 10^{-8}(T-298)^2$
6.9	298–730	$a(T) = 5.1684 + 2.758 \times 10^{-5}(T-298) + 1.992 \times 10^{-8}(T-298)^2$
12.7	298–615	$a(T) = 5.1684 + 3.195 \times 10^{-5}(T-298) + 3.277 \times 10^{-8}(T-298)^2$

The estimated standard deviation in $a(T)$ is <0.0009 Å at a given temperature and electric field. The r^2 of all nonlinear regressions in Fig. 3 is >99.5%.

Results and discussion

Figure 2 shows the room temperature energy-dispersive X-ray diffraction (EDXRD) pattern of the as-received nano-B_4C powder as a function of energy for 2θ = 3° diffraction angle under zero–electric field condition. By using this pattern, we determined the room temperature and zero-field lattice parameter (a_R) and unit cell angle of rhombohedral (δ_R) of nano-B_4C as a_R = 5.1684 (0.0009) Å and δ_R = 65.7046° (0.0007); respectively, where the numbers within parentheses indicate the standard deviation.

Figure 3 depicts the variation of the rhombohedral unit cell parameter of nano-B_4C as a function of temperature (K) and under various applied DC electric fields. One observes that a_R increases monotonously with increasing temperature. The variation of a_R with the temperature at zero–electric field was found to be nonlinear (parabolic), which is curious because the temperature range of interest is well below the melting temperature (2763 °C). Typically, one would expect a deviation from linearity as the melting temperature is approached on heating. In addition, we also observed that the variation of the lattice parameter exhibited an electric field dependence as can be verified in Fig. 3. Moreover, we observed that the variation of the lattice parameter with temperature becomes more nonlinear as the applied DC electric field strength is increased (see Fig. 3).

On the other hand, the rhombohedral angle (δ_R) of B_4C was found to be invariant [65.7046° (0.0007)] with respect to temperature, as well as the applied DC electric field intensity as shown in Fig. 4. The observed invariance of the rhombohedral angle indicates that the unit cell expansion must be hydrostatic. As such, the symmetry of the unit cell expansion under the action of both temperature and applied DC electric field is spherical, i.e., Curie group ∞∞m [2]. This result is surprising because the rhombohedral unit cell belongs to the uniaxial family of crystals for which the thermal expansion matrix has two nonvanishing and unequal

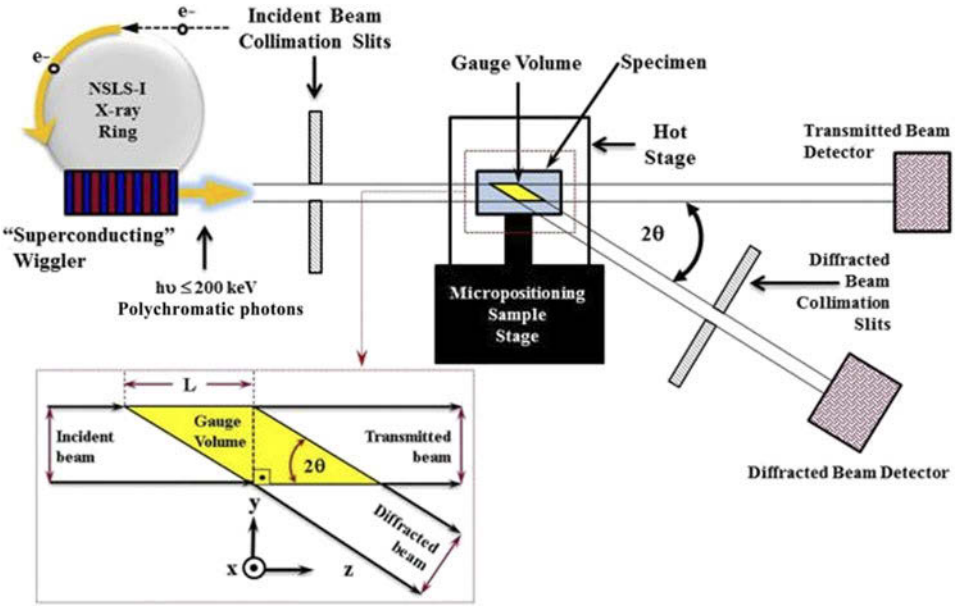

Figure 2: Room temperature zero–electric field energy-dispersive X-ray synchrotron diffraction spectrum of as-received nano-B_4C.

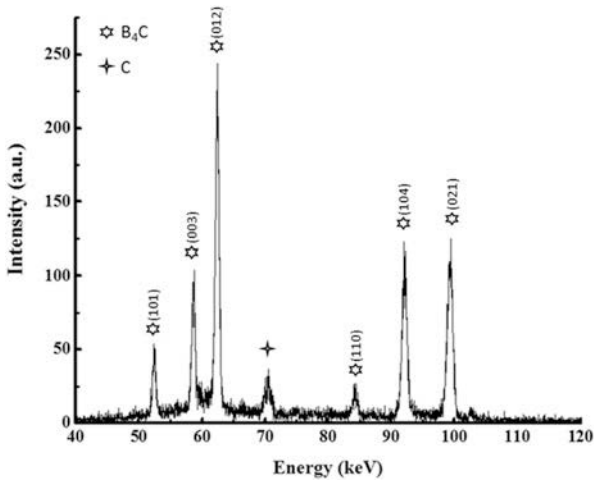

Figure 3: Variation of the nano-B_4C rhombohedral unit cell parameter as a function of temperature (K) under various applied DC electric field strengths.

second rank tensor elements, i.e., $\alpha_{11} = \alpha_{22} \neq \alpha_{33} \neq 0$ and $\alpha_{ij} = \alpha_{ji} = 0$ for $i \neq j$, where $i, j = 1, 2, 3$ [23]. Normally, an increase in temperature should cause a change in the rhombohedral angle because $\alpha_{11} \neq \alpha_{33} \neq 0$, where α_{33} represents the expansion along the body diagonal of the rhombohedral unit cell. Such anisotropy is absent in the zero-field variation of the δ_R and nonzero-field variation of δ_R in nano-B_4C. Therefore, the experimental results suggest that the anisotropic characteristic of thermal expansion appears to be lost in nano-B_4C with or without an applied DC electric field. The variation of the unit cell volume of the nano-B_4C rhombohedral unit cell is shown in Fig. 5. The effect of temperature and applied DC electric field on the unit cell volume parallels the behavior of the lattice parameter because the unit cell angle was found to be invariant as expounded in the preceding discussion. The said variation is also parabolic despite the fact that the temperature range of interest is well below the melting temperature.

The results of the appertaining temperature dependence of the rhombohedral lattice parameters of nano-B_4C at various applied DC electric fields are summarized in Table I, from which the TEC and its electric field dependence were obtained. The application of Eqs. (1)–(4) to the data reported in Table I enabled us to obtain α_1 and α_2 in the range 0–12.7 V/mm, where α_1 is the zeroth-order TEC, while α_2 is the first-order TEC for rhombohedral nano-B_4C, which are functions of electric field as well, as shown in Fig. 6. From the data in Fig. 6 in conjunction with the data in Table I, we obtain the zero–electric field $\alpha_1(E_o = 0)$ and $\alpha_2(E_o = 0)$ as $4.822 \pm 0.003 \times 10^{-6}$ K^{-1} and $1.461 \pm 0.008 \times 10^{-9}$ K^{-1}, respectively. A close look at Fig. 6 also reveals that both $\alpha_1(E)$ and $\alpha_2(E)$ exhibit nonlinear variation with applied DC electric field strength. However, the nonlinearity is more pronounced in zeroth-order TEC ($\alpha_1(E)$) than in the first-order TEC ($\alpha_2(E)$).

The analytical form of the electric field dependence of $\alpha_1(E)$ and $\alpha_2(E)$ was obtained by a Taylor expansion, which we truncated at the second order (parabolic) term using

$$\alpha_1(E) \approx \alpha_1(E_o) + \Theta_1^1(E - E_0) + \Theta_1^2(E - E_0)^2 \qquad (6a)$$

$$\alpha_2(E) \approx \alpha_2(E_o) + \Theta_2^1(E - E_0) + \Theta_2^2(E - E_0)^2 \qquad (6b)$$

where $E_o = 0$ V/mm, and the Θ coefficients are defined as

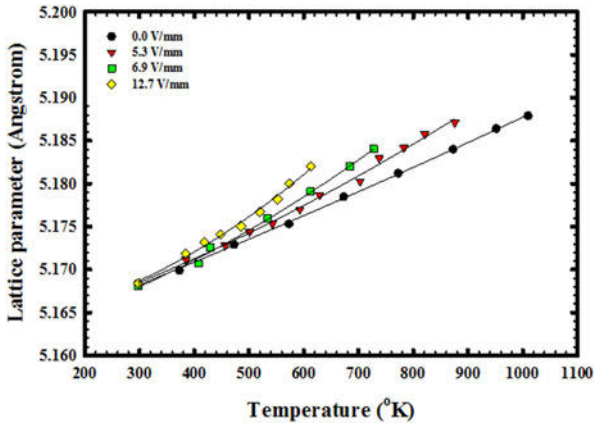

Figure 4: Variation of the rhombohedral angle (δ_R) of B_4C as a function of temperature (K) under various applied DC electric field strengths.

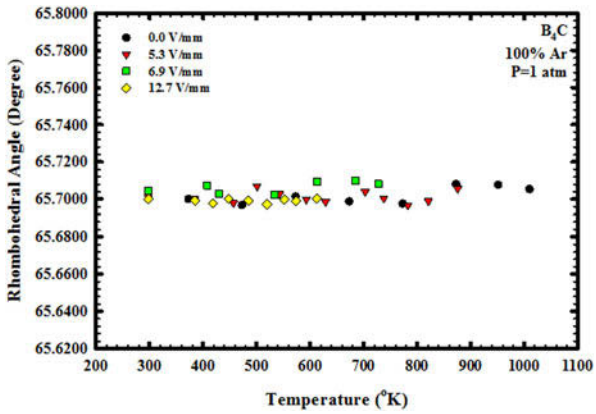

Figure 5: Variation of the unit cell volume of the rhombohedral B_4C as a function of temperature and applied DC electric field.

$$\Theta_1^1 = \left(\frac{\partial \alpha_1(E_o)}{\partial E}\right) \text{ and } \Theta_1^2 = \left(\frac{1}{2!}\frac{\partial^2 \alpha_1(E_o)}{\partial^2 E}\right)$$
$$\Theta_2^1 = \left(\frac{\partial \alpha_2(E_o)}{\partial E}\right) \text{ and } \Theta_2^2 = \left(\frac{1}{2!}\frac{\partial^2 \alpha_2(E_o)}{\partial^2 E}\right) \quad . \qquad (6c)$$

The results of the electric field dependence of $\alpha_1(E)$ and $\alpha_2(E)$ are summarized in Table II.

The zeroth-order TEC (α_1 at $E_o = 0$) obtained in this study is in reasonable agreement with the values reported in the literature [14]. There is also a first-order TEC response (α_2 at $E_o = 0$) of nano-B_4C despite the temperature range that we probed is less than 50% of the melting temperature. Although we have used 6 Bragg reflections for obtaining (a_R, δ_R) for the nano-B_4C's rhombohedral unit cell, we did not observe any anisotropic thermal expansion as evidenced by the invariance of δ_R with both temperature and applied DC electric field strength. At the first glance, one might be inclined to hypothesize that the observed isotropic thermal expansion is due to some polycrystalline averaging. However, the particle size of nano-B_4C particles is simply too small to accommodate

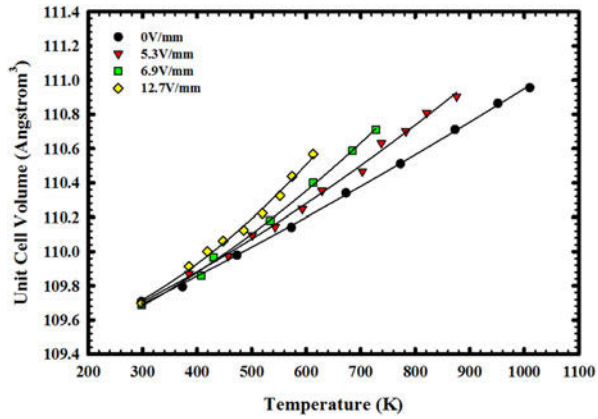

Figure 6: Variation of TECs with applied DC electric field strength: (a) zeroth-order TEC ($\alpha(E)$) and (b) first-order TEC ($\alpha_2(E)$) for nano-B_4C.

TABLE II: Applied DC E dependence of zeroth- and first-order TECs in nano-B_4C.

	$\alpha_1(E_o = 0)$ (1/K)	Θ_1^1 [(mm/V)/K]	Θ_1^2 [(mm/V)^2/K]
$\alpha_1(E)$	$4.822 \pm 0.003 \times 10^{-6}$	$3.30 \pm 0.04 \times 10^{-8}$	$5.80 \pm 0.05 \times 10^{-9}$
	$\alpha_2(E_o = 0)$ (1/K)	Θ_2^1 [(mm/V)/K]	Θ_2^2 [(mm/V)^2/K]
$\alpha_2(E)$	$1.461 \pm 0.008 \times 10^{-9}$	$6.19 \pm 0.07 \times 10^{-10}$	$2.15 \pm 0.08 \times 10^{-11}$

The r^2 of all nonlinear regressions in Fig. 7 is >99.5%.

enough crystallites with independent orientational variants in their volumes. We also rule out the impact of the applied DC electric field on the observed isotropic thermal expansion because it is observed under zero–electric field condition as well. Hence, we are led to conclude that the isotropic thermal expansion is related to the nanosize of B_4C by virtue of the fact that the surface-to-volume ratio is very high. The said surface is well known to act as sources and sinks for defects. Above all, B_4C possesses a very complicated defect structure, which is still debated [24]. Furthermore, our results on the constancy of the rhombohedral angle (under zero–electric field conditions) match remarkably well with the data reported for carbon-saturated B_4C by Yakel [25]. Yakel reports a rhombohedral angle of 65.69–65–70° over a temperature of 12–945 °C, whereas the same was obtained as 65.7046° (0.0007) in this study. Therefore, we conjecture that the observed anomaly (isotropic thermal expansion) in rhombohedral B_4C also has a stoichiometric dimension that should be directly linked to its defect chemistry in principle [24, 25].

Turning to the impact of the applied DC electric field, we have shown that the thermal expansion temperature coefficient becomes larger with increasing applied field strength. As is known, the magnitude of the TEC is related to the curvature of the interatomic potential and $r = r_o$, where r_o is the average interatomic spacing in the solid of interest at a given temperature [1]. Therefore, we postulate that the applied DC electric

field decreases the curvature of the interatomic potentials in nano-B_4C, thereby increasing the TECs $\alpha_1(E)$ and $\alpha_2(E)$ based on the experimental findings reported herein. This, in turn, implies that the applied DC electric field increases the asymmetry of the interatomic potentials in nano-B_4C, thereby inducing a lattice softening [26].

Conclusions

By using an advanced in situ XRD method in conjunction with a self-consistent data analysis and reduction protocol, we have assessed the thermal expansion behavior of nano-B_4C having 50 nm mean particle size as a function of applied DC electric field. We have shown that the zeroth- and first-order TEC coefficients exhibit parabolic applied DC electric field dependence, whereas the thermal expansion of the rhombohedral unit cell loses its anisotropic nature. We have shown that the thermal expansion behavior of such nano-B_4C deviates from the expected bulk behavior. Hence, we conjecture that the observed deviations from bulk behavior are related to B_4C being in the nano-phase with a medium particle size of 50 nm. However, the effects of carbon saturation on the observed thermal expansion behavior cannot be disregarded.

It may be very useful if the approach presented herein is extended to other highly covalent nano-size ceramics exhibiting insulator behavior in a given temperature range and over a range of applied electric field strengths. Such studies will most likely enable one to shed light on nano-phase behavior in such low atomic mobility systems.

Experimental methods

Nano-B_4C characteristics

The nano-B_4C powder, which was used in this study, was supplied by the U. S. Army Armament Research, Development and Engineering Center at Picatinny Arsenal, New Jersey, USA [27]. The nano-B_4C powder had a 50 nm median particle size. The powder did not require additional powder processing such as grinding and milling. The as-received powder was uniaxially pressed without a binder into cylindrical pellets of 12 mm diameter and 2.5 mm thickness. The apparent densities of the uniaxially pressed pellets, which we simply determined from their masses and volumes, were 60–65% of the X-ray density.

X-ray diffraction method

The in situ diffraction work reported here was conducted at the superconducting wiggler X17-B1 beamline in the National Synchrotron Light Source (NSLS I) at the Brookhaven National Laboratory (BNL), Upton, New York. Ultrahigh energy polychromatic radiation with photons as energetic as 200 keV was used for EDXRD. Figure 7 depicts a schematic illustrating for the diffraction technique of interest. The said technique is essentially a Laue method (also known as the transmission method) in which the specimen under test is stationary [20]. The stationary nature of this transmission technique allows one to carry out in situ experiments that are otherwise not possible with conventional Bragg–Brentano diffraction methods (surface- and/or subsurface-specific methods). The technique involves an ultrahigh energy polychromatic incident radiation that is scattered at a fixed Bragg angle. The intensity of the scattered radiation is measured by a germanium detector [20]. The incident and scattered beam collimating slit openings and the fixed Bragg angle define the gauge volume (GV) which is fixed in space. The specimen is translated so that it overlaps with the GV at which point the GV becomes the diffraction volume. The size of the diffraction volume is chosen such that it accommodates an abundance of randomly oriented nano-B_4C particles, ensuring proper particle statistics. Because the diffraction data originate from the bulk of the specimen, it is not prone to potential complications arising from the specimen's surface and/or subsurface.

A custom-made hot stage (HS) was used to heat the sample while a DC electric field was applied to the specimen in the parallel plate capacitor geometry as described elsewhere [20]. The HS comprised a spring loaded ceramic (insulator) specimen holder that is resistively heated by applying the electric field using a power supply (Power Designs Inc—Model 6150—Universal DC Power Source) [20]. The HS enclosure is mounted on the positioning stage (see Fig. 7) and then exposed to the beam. The GV is then carefully placed on the body center of the specimen and is then resistively heated with a nominal heating rate of 30 °C per minute. Meanwhile, an applied DC electric field in the range 0–12.7 V/mm was imposed on the specimen using a second power supply (BK Precision—Model 9115—Multi Range DC Power Supply), and the temperature and leakage current were monitored. A full X-ray spectrum was collected every 2–3 s, which resulted in the collection of over 400 spectra for each electric field strength from which representative ones were chosen for analysis. An inert gas dynamic atmosphere (argon) protected the specimen from oxidation.

The governing equation for EDXRD, which was used in the ensuing data analysis, is provided herein for completeness as follows: The Bragg's law $n\lambda = 2d_{hkl}\sin\theta_{hkl}$ (here, n is the order of reflection and λ is the wavelength of the radiation) is combined with the Planck–Einstein equation $E = h\nu$, with $\nu = c/\lambda$ (here, ν is the linear frequency), and setting $n = 1$, to obtain [20].

$$\frac{1}{d_{hkl}} = \left(\frac{2\sin\theta_{hkl}}{hc}\right)E_{hkl} = |Q_{hkl}| \quad , \tag{7}$$

where d_{hkl} is the interplanar spacing of the atomic plane with Miller indices (hkl), θ is the Bragg angle which is kept constant

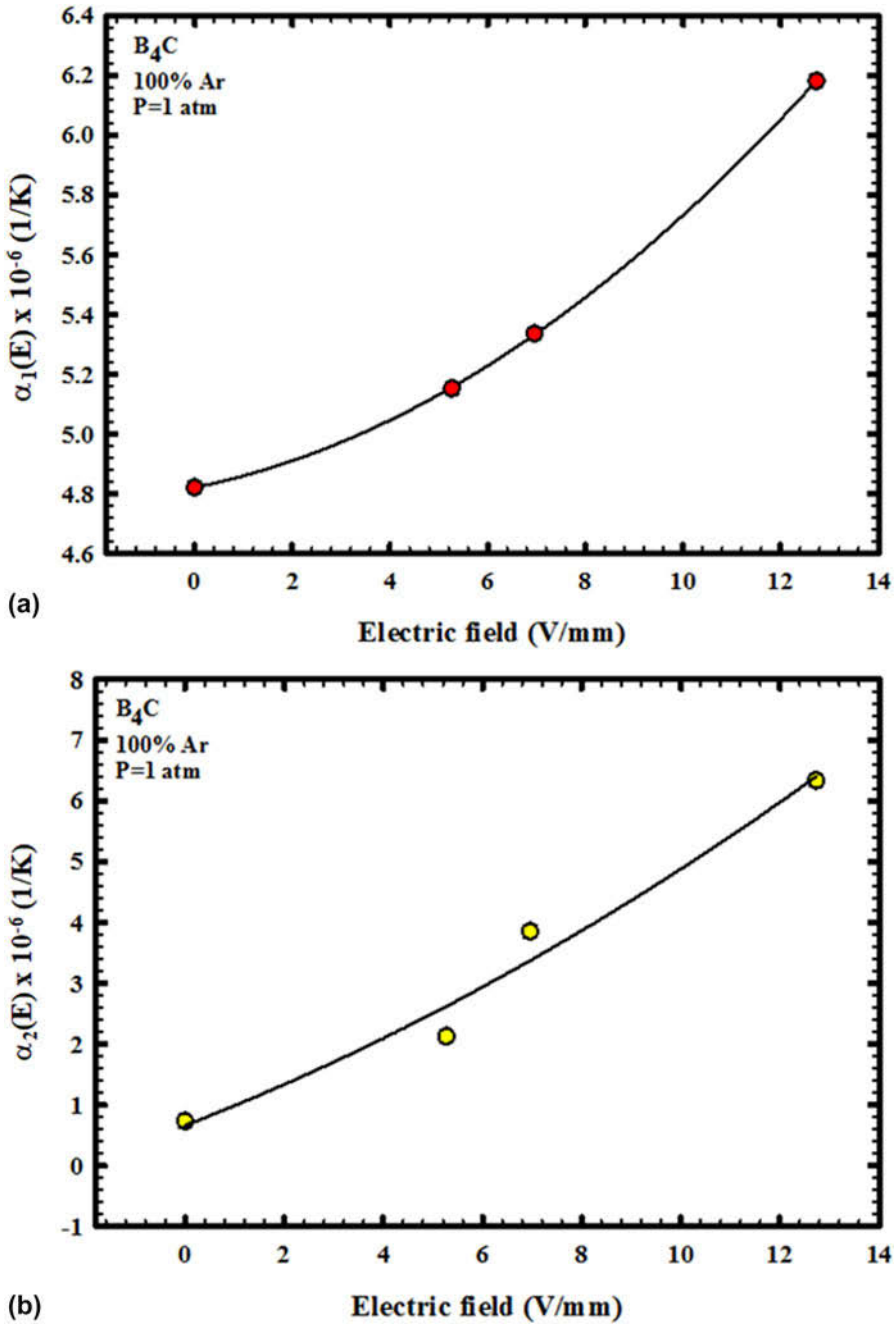

Figure 7: Schematic summarizing the EDXRD method used at the X17-B1 superconducting wiggler beamline, National Synchrotron Light Source, Brookhaven National Laboratory. The method is based on a transmission technique with a fixed GV in 3D space. The inset is a ray diagram depicting the relationships between incident, diffracted, and transmitted beams, and the relationship between the gauge length (L) and the Bragg angle (θ), which is kept constant in the EDXRD method.

at 1.5°. In this study, h is Planck's constant (6.626×10^{-34} J s), c is the speed of light (2.9979×10^{8} m/s), E_{hkl} is the scattered energy from lattice plane (hkl), and $|Q_{hkl}|$ is the magnitude of the reciprocal lattice vector pertaining to (hkl) in reciprocal space [20]. Here, E_{hkl} is the measured quantity, which is equivalent to measuring the magnitude of the reciprocal lattice vector Q_{hkl} directly [see Eq. (7)], thereby enabling one to determine d_{hkl} with great accuracy. The energy calibration was accomplished by using Ag, Au, Cu, CeO_2, TiO_2, and LaB_6 (NIST SRM 660) standards. A pseudo-Voigt profile shape function was used to measure the peak centroids [28, 29]. Diffraction data were collected at 0.0 V/mm, 5.3 V/mm, 6.9 V/mm, and 12.7 V/mm applied electric field intensities (accuracy ±0.5–1%), and over a range of temperatures spanning from room temperature to 1010 °K, 875 °K, 730 °K, and 615 °K, respectively. The accuracy of the temperature measurement is

estimated as ±3 °C. In each experiment, we ascertained that no current flow occurred across the specimen for a given applied DC electric field strength over the temperature range of the measurement. In so doing, we ensured what was measured represented the TEC as defined in Eq. (2).

Acknowledgments

The authors wish to express their gratitude for the financial support provided by the Office of Naval Research (ONR) under Contract Nos. N00014-10-1-042 and N00014-17-1-2087, Sub-Award No. 4104–78982 from Purdue. The authors wish to thank Dr. Antti Makinen and Dr. Larry Kabacoff of the ONR for their valuable technical feedback. This research was carried out in part at the NSLS, which is supported by the U.S. Department of Energy, Division of Material Sciences, and Division of Chemical Sciences, under Contract No. DE-AC02-06CH11357. H.B. and İ.Ş. acknowledge the financial support from the Ministry of Education of the Turkish Republic.

References

1. **C. Kittel**: *Introduction to Solid State Physics*, 8th ed. (John Wiley & Sons, New York, NY, 2005).
2. **R.E. Newnham**: *Properties of Materials* (Oxford University Press, Oxford, U.K., 2005).
3. **V. Domnich, S. Reynaud, R.A. Haber, and M. Chhowalla**: Boron carbide: Structure, properties, and stability under stress. *J. Am. Ceram. Soc.* **94**, 3605–3628 (2011).
4. **R.A. Andrievski**: Micro- and nanosized boron carbide: Synthesis, structure and properties. *Russ. Chem. Rev.* **81**, 549–559 (2012).
5. **N. Vast, J. Sjakste, and E. Betranhandy**: Boron carbides from first principles. *J. Phys.: Conf. Ser.* **176**, 012002 (2009).
6. **A.K. Suri, C. Subramanian, J.K. Sonber, and T.C. Murthy**: Synthesis and consolidation of boron carbide: A review. *Int. Mater. Rev.* **55**, 4–40 (2010).
7. **C. Wood and D. Emin**: Conduction mechanism in boron carbide. *Phys. Rev. B* **29**, 4582 (1984).
8. **B. Matchen**: Applications of ceramics in armor products. *Key Eng. Mater.* **122**, 333–344 (1996).
9. **L. Vargas-Gonzalez, R.F. Speyer, and J. Campbell**: Flexural strength, fracture toughness, and hardness of silicon carbide and boron carbide armor ceramics. *Int. J. Appl. Ceram. Technol.* **7**, 643–651 (2010).
10. **D. Emin and T.L. Aselage**: A proposed boron-carbide-based solid-state neutron detector. *J. Appl. Phys.* **97**, 013529 (2005).
11. **W.K. Barney, G.A. Sehmel, and W.E. Seymour**: The use of boron carbide for reactor control. *Nucl. Sci. Eng.* **4**, 439–448 (1958).
12. **B.D. Cullity**: *Elements of X-ray Diffraction*, 2nd ed. (Adisson-Wesley Publishing, USA, 1978).
13. **T.L. Aselage and R.G. Tissot**: Lattice constants of boron carbides. *J. Am. Ceram. Soc.* **75**, 2207–2212 (1992).
14. **F. Thevenot**: Boron carbide—A comprehensive review. *J. Eur. Ceram. Soc.* **6**, 205–225 (1990).
15. **A. Lipp**: *Boron Carbide: Production, Properties, and Applications*, Battelle Northwest Laboratories, NTIS Issue Number 197013, 1970.
16. **T.R. Pilladi, G. Panneerselvam, S. Anthonysamy, and V. Ganesan**: Thermal expansion of nanocrystalline boron carbide. *Ceram. Int.* **38**, 3723–3728 (2012).
17. **O. Guillon, J. Gonzalez-Julian, B. Dargatz, T. Kessel, G. Schierning, J. Räthel, and M. Herrmann**: Field-assisted sintering technology/spark plasma sintering: Mechanisms, materials, and technology developments. *Adv. Eng. Mater.* **16**, 830–849 (2014).
18. **U. Anselmi-Tamburini, Z.A. Munir, Y. Kodera, T. Imai, and M. Ohyanagi**: Influence of synthesis temperature on the defect structure of boron carbide: Experimental and modeling studies. *J. Am. Ceram. Soc.* **88**, 1382–1387 (2005).
19. **D. Yang, R. Raj, and H. Conrad**: Enhanced sintering rate of zirconia (3Y-TZP) through the effect of a weak dc electric field on grain growth. *J. Am. Ceram. Soc.* **93**, 2935–2937 (2010).
20. **E.K. Akdoğan, İ. Şavklıyıldız, H. Biçer, W. Paxton, F. Toksoy, Z. Zhong, and T. Tsakalakos**: Anomalous lattice expansion in yttria stabilized zirconia under simultaneous applied electric and thermal fields: A time-resolved in situ energy dispersive X-ray diffractometry study with an ultrahigh energy synchrotron probe. *J. Appl. Phys.* **113**, 233503 (2013).
21. **T.J.B. Holland and S.A.T. Redfern**: Unit cell refinement from powder diffraction data: The use of regression diagnostics. *Mineral. Mag.* **61**, 65–77 (1997).
22. **Y. Waseda, E. Matsubara, and K. Shinobada**: *X-ray Diffraction Crystallography* (Springer, New York, 2011).
23. **J.F. Nye**: *Physical Properties of Crystals* (Oxford University Press, Oxford, U.K., 1985).
24. **M.M. Balakrishnarajan, P.D. Pancharatna, and R. Hoffmann**: Structure and bonding in boron carbide: The invincibility of imperfections. *New J. Chem.* **31**, 473 (2007).
25. **H.L. Yakel**: Lattice expansions of two boron carbides between 12 and 940 °C. *J. Appl. Crystallogr.* **6**, 471 (1973).
26. **M. Born and K. Huang**: *Dynamical Theory of Crystal Lattices* (Clarendon Press, Wotton-Under-Edge, 1998).
27. **C. Haines, E.K. Akdoğan, and T. Tsakalakos**. Private communication (2019).
28. **R.L. Snyder:** *The Rietveld Method*, R.A. Young, ed. (Oxford University Press, New York, NY, 1993); pp. 111–131.
29. Jade (Materials Data Inc., Livermore, California, 2019).